1

> Banner appropriate to article type will appear here in typeset article

Effect of singularity on the dynamics of a collapsing bubble in contact with a rigid wall

Mandeep Saini[1]†, Erwan Tanne[2], Michel Arrigoni [2], Stephane Zaleski [1,3] and Daniel Fuster[1]‡

[1]Sorbonne Université and CNRS UMR 7190, Institut Jean le Rond ∂'Alembert F75005 Paris, France

[2]ENSTA Bertagne UMR 6027 - IRDL F-29806, Brest, France

[3]Institut universitaire de France, UMR 7190, Institut Jean le Rond ∂'Alembert F75005 Paris, France

This work reveals that the dynamic response of a bubble in contact with a rigid wall depends on the effective contact angle at the instant prior to collapse. For contact angles larger than 90 degrees the potential flow is singular at the contact line leading to the appearance of a annular re-entrant jet parallel to the wall and modifying the mechanisms of interaction between the collapsing bubble and its surrounding medium. Numerical and experimental results show that in these circumstances it is possible to observe the formation of a vortex ring that unexpectedly induces long range interactions between the bubble and a free surface. Our results provide a significant step forward towards the understanding of this fundamental problem with direct implications in underwater volcano eruptions as well as the control and design of biological, medical, naval, manufacturing and sonochemistry applications.

MSC Codes *(Optional)* Please enter your MSC Codes here

1. Introduction

Cavitation, the process of bubble formation and collapse is a key physics problem because of its applications in nature, mechanics, biomedical, and many other fields (**??????**). Bubbles generally appear from nuclei sitting at walls (**???**), making the interaction with the wall an essential aspect of bubble collapse dynamics. The wall modifies the symmetry of the pressure field near the bubble that causes unequal interface acceleration and thus high-speed liquid jets and leads to complex cavitation phenomena (**???**). These jets are important to understand the destructive potential of the cavitation bubbles for several biomedical applications such as the disruption of biological membranes in High Intensity Focussed Ultrasound (HIFU), lithotripsy, histotripsy and sonoporation techniques (**???**). Other applications concerning

† mandeep.saini@sorbonne-universite.fr
‡ Email address for correspondence: dfuster@gmail.com

Abstract must not spill onto p.2

erosion, surface cleaning, noise emission and manufacturing processes (e.g. shotpeening) are also closely linked to the phenomenon of jetting (??). The bottleneck in development of these techniques remains the limited understanding of the interaction of cavitation bubble with its surrounding medium.

It is well known that the jets formed during the collapse of bubbles in the presence of a nearby wall are directed towards the wall that can be described well using the scaling laws given by ?. However, the investigations on the collapse of a bubble, initially attached to a wall are reported less often (???) and many aspects remain unexplored. In particular, ? speculate the appearance of a jet parallel to the wall during the secondary collapse, although no direct experimental observation is reported. Similar behaviour has also been observed in numerical simulations of ??, but the explanations about the origin of such phenomena was not described.

In this article we bridge this gap and describe the factors controlling the jetting direction using comprehensive theoretical, numerical and experimental evidences. We clarify that the change in the jetting direction is an implication of the singularity in pressure gradient when obtained from the potential flow model. This singularity only appears when the effective contact angle at the instant before the collapse (α) is larger than 90 degrees. We show that at short instants after begining of collaspe phase and for sufficiently large Reynolds and Weber numbers, the potential flow solution provides accurate predictions of the bubble response obtained from the direct numerical solution of the Navier–Stokes equations. Despite the fact that viscosity instantaneously regularizes the solution near the singularity and predicts finite velocities, the effect of singularity is still present outside the boundary layer and it explains the changes in the nature of the jet generated. In addition, we show that there is a direct link between the bubble response at small times and the formation of vortex ring that eventually leads to surprising long range interaction effects between the bubble and a free surface that have not been reported before. These results provide a significant advance in the characterization of the interaction mechanisms between a bubble and its surrounding medium and may be behind unexplained delayed effects in underwater explosions observed by ? and tsunami generation by underwater volcano eruptions (?).

2. Problem setup

We focus on the classical three-dimensional Rayleigh collapse problem for bubble that has a spherical cap shape (figure 1). We restrict ourselves to an axisymmetric configuration where the initial bubble pressure p_0 is uniform inside the bubble and the liquid, initially at rest, is at a higher pressure far from the bubble $p_\infty > p_0$. This problem represents the solution of a bubble in equilibrium state subjected to impulsive action caused by a sudden increase in far-field pressure, and also the dynamic response of a low pressure bubble after the expansion stage when it reaches its maximum radius and the liquid velocity is approximately zero.

The dynamics of this system is governed by the mass, momentum and energy conservation laws, which for the ith component in a multi-component setup is given as

$$\frac{\partial \rho_i}{\partial t} + \nabla \cdot (\rho_i \mathbf{u}) = 0, \tag{2.1a}$$

$$\frac{\partial \rho_i \mathbf{u}}{\partial t} + \nabla \cdot (\rho_i \mathbf{u}u) = -\nabla p + \nabla \cdot \tau_i, \tag{2.1b}$$

$$\frac{\partial (\rho_i E_i)}{\partial t} + \nabla \cdot (\rho_i E_i) = -\nabla \cdot (\mathbf{u}p) + \nabla \cdot (\tau'_i \mathbf{u}). \tag{2.1c}$$

As usual, $\mathbf{u}$ represents the velocity vector field, ρ is density, p is the pressure field and the viscous stress tensor for each component is written as $\tau_i = \mu_i(\nabla \mathbf{u} + (\nabla \mathbf{u})^{\mathrm{T}})$. The total energy

Figure 1: (a) Problem setup and different coordinate systems used in this article

$\rho_i E_i = \rho_i e_i + \frac{1}{2}\rho_i \mathbf{u} \cdot \mathbf{u}$, is the sum of internal energy per unit volume $\rho_i e_i$ and kinetic energy $\frac{1}{2}\rho_i \mathbf{u} \cdot \mathbf{u}$ per unit volume. Finally the equation of state (EOS) is written as $\rho_i e_i = \frac{p_i + \Gamma_i \Pi_i}{\Gamma_i - 1}$ where Γ and Π are adopted from Johnsen & Colonius (**?**) in such a way that liquid is a slightly compressible and the bubble content obeys an ideal gas EOS. The system of equations is closed by adding an advection equation for the interface position.

In the full DNS, a non-slip boundary condition is imposed for the velocity field a the wall, while a standard free flow condition is applied in all the other boundaries. Note that although a non-slip boundary condition imposes zero velocity at the boundary, the velocity at which the interface is advected in the cell adjacent to the wall is different from zero which effectively acts as an implicit slip length for the contact line motion given as $\lambda = \Delta_{min}/2$, where Δ_{min} is the smallest grid size. The static contact angle model proposed by Afkhami and Bussamann is employed to implement contact angle boundary condition **?** which, although not very accurate for prediction the contact line motion, is a handy tool that gives fair insight of the growth of boundary layer and range of influence of viscosity. More sophisticated models could be used but a significant change in the conclusions of this work is not expected.

The initial conditions are defined by imposing the fluid to be initially at rest ($\boldsymbol{u} = 0$). In this case we can take the divergence of the momentum equation while assuming the liquid as an incompressible substance to obtain a Laplace equation for the liquid pressure,

$$\Delta p = 0. \tag{2.2}$$

This equation is readily solved if we assume that the gas pressure is initially uniform such that the boundary conditions for pressure (as shown in figure 1a) are the following: at the interface the liquid pressure is

$$p_{0,L} = p_0 - \frac{2\sigma}{R_c}, \tag{2.3}$$

where σ is the surface tension coefficient and R_c is the radius of curvature; at the far–away boundaries the pressure is p_∞ and at the wall the normal pressure gradient is null due to impermeability condition. The initial condition for total energy is then calculated from the EOS using the initial pressure field.

We finally introduce relevant dimensionless quantities using the radius of curvature as characteristic length, the liquid density and the characteristic velocity $U_c = (p_\infty/\rho_l)^{1/2}$ obtained by assuming that at the instant of maximum radius the liquid pressure along the surface is negligible compared to the far–field pressure. This velocity is 10 m/s at atmospheric conditions. By simple dimensional analysis the solution of the problem depends on the density and viscosity ratios, the Reynolds number, $Re = \frac{\rho_l U_c R_c}{\mu_l}$, the Weber number $We = \frac{\rho_l U_c^2 R_c}{\sigma}$ and the contact angle (α). In this work we limit our investigations to bubbles with a radius
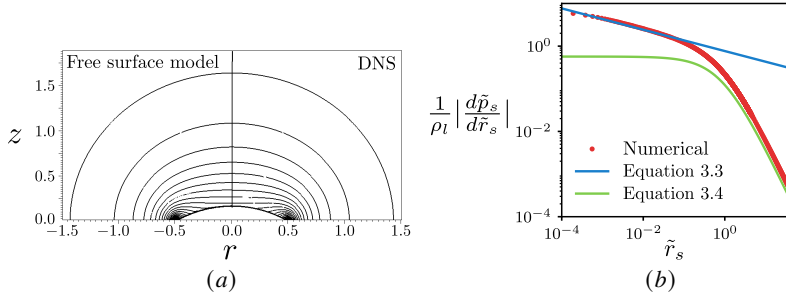
Figure 2: (a) Problem setup and different coordinate systems used in this article (b) Isocontours of the magnitude acceleration for bubble with contact angle $\alpha = 2\pi/3$: The left half isocontours are obtained from free surface model and in the right half isocontours are obtained from DNS with infinite Reynolds. (c) Non-dimensional acceleration magnitude along the wall obtained for bubble with contact angle $\alpha = 2\pi/3$ using the free surface model.

of curvature of the order of larger than 1 cm obtaining characteristic values of the Weber and Reynolds number of the order of $We \sim O(10^3)$ and $Re \sim O(10^4)$.

3. Short time dynamics

At short times, we can simplify the system of equations if we consider the interface as a free surface, i.e. we neglect inertial and viscous effects inside the bubble, which is a reasonable assumption given that $\mu_g/\mu_l \ll 1$ and $\rho_g/\rho_l \ll 1$ (in experiments the density ratio is of the order of 10^{-5} when the bubble pressure equals the vapor pressure). The velocity at small times remains a small quantity, thus we can neglect the convective terms as compared to temporal derivatives of velocity and spatial pressure gradients (**?**). This hypothesis remains true when time scales under consideration are smaller than the advection time scales i.e. $\frac{t_s U_c}{R_c} \ll 1$. Under these assumptions the solution of the velocity is obtained from the integration of the linearized momentum equation as

$$\mathbf{u}(t_s) = -\frac{1}{\rho}\int_0^{t_s}\nabla p + \frac{1}{\rho}\int_0^{t_s}\nabla\cdot\tau. \tag{3.1}$$

It is classical for this linear system to decompose the velocity field into a potential part (u_ϕ) and a viscous correction (u_ν) i.e. $u = u_\phi + u_\nu$. The potential flow theory gives u_ϕ whereas the viscous correction requires complex analysis (**???**). For the short times and large enough Reynolds numbers, the viscous contributions to velocity are relevant only in the small region of thickness $\delta \sim O(\sqrt{\nu t})$ near the solid boundary. Thus for large Reynolds and short times, we expect the solution to be governed by the potential part, the viscous part being only a correction in a thin region close to the wall. We discuss these aspects next.

3.1. *Potential flow solution*

The potential flow solution is obtained by solving the inviscid part of the linearized momentum equation

$$\frac{\partial\mathbf{u}_\phi}{\partial t} = -\frac{1}{\rho}\nabla p.$$

The magnitude of pressure gradient field (or acceleration field) at short infinitesimal times govern the dynamics of bubble collapse at a finite time. To obtain the acceleration we introduce the dimensionless pressure $\tilde{p} = \frac{p - p_{0,L}}{p_\infty - p_{0,L}}$. Note that in the linear problem the
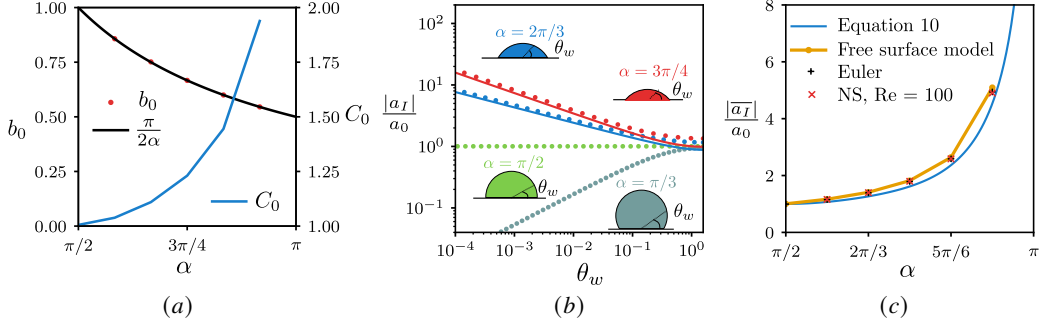
Figure 3: (a) Exponent b_0 and coefficient C_0 obtained from fitting the pressure gradient obtained from the free surface model along the wall for different contact angles at wall α. (b) Non-dimensional acceleration magnitude, $|a|_I/a_0$ along the interface parametrized using the angle θ_w (measured in the counter-clockwise direction from the point of contact of wall and the bubble) for $\alpha = \frac{\pi}{3}, \frac{\pi}{2}, \frac{2}{3}\pi, \frac{3}{4}\pi$. Dots represent the numerical solution from free surface model and the thick lines are predictions using Eq. 3.3 evaluated at the interface. (c) Nondimensional averaged interface acceleration magnitude as a function of the contact angle using different methods: analytical expression given by Eq. 3.5 (blue line), the solution from the free surface model (yellow line), the DNS solution of the Euler equations (black crosses), and the DNS solution of the Navier–Stokes solver for $Re = 100$ (red crosses).

128 interface does not move, therefore surface tension effects at short times only introduce
129 a correction on the scaling prefactor $p_\infty - p_{0,L}$ upon which the solution depends. The
130 boundary conditions required to solve the Laplace equation (Equation 2.2) for $\tilde{p}$ are: $\tilde{p} = 1$
131 far away from the bubble, $\tilde{p} = 0$ at the bubble interface and homogeneous Neumann at the
132 solid boundary. The solution of this equation depends only on the geometry of the bubble.
133 For a bubble initially at rest, the dimensionless solution of the problem depends only on the
134 contact angle (α). This simplified representation of the fluid fields at short times is referred
135 as 'free surface model' in this article.
136   In figure 2a, we start presenting the isocontours of the magnitude of the non-dimensional
137 acceleration ($|\frac{1}{\rho}\nabla\tilde{p}|$) field obtained for a spherical cap bubble with contact angle $\alpha = \frac{2}{3}\pi$
138 while figure 2b shows the variation of same along the wall in the liquid phase with respect
139 to the distance from the contact line obtained from free surface model. The isocontours
140 in the left half are obtained numerically from the free surface model, while on the right
141 half are obtained from the full Direct Numerical Simulation (DNS) of the Navier–Stokes
142 equations accounting for the presence of a gas with non-zero density and a finite value
143 of viscosity at $\frac{tU_c}{R_c} = 2.07 \cdot 10^{-6}$. Good agreement between the two models supports the
144 argument that equation 2.2 is a good representation of the fluid dynamics at very short
145 times. We clearly distinguish two separate regions: the far-field where the pressure gradient
146 contours are hemispherical caps centered at the axis of symmetry, and the near field where
147 the contours for pressure gradient are intricate and diverge on approaching the triple contact
148 point. Next, we characterize each of these regions:

149 ### 3.1.1. *Near field*

150 The general solution of the Laplace equation in spherical coordinates can be obtained by
151 sepration of variables that leads to an infinite series. This series sometimes diverges at the
152 edge where Dirichlet and Neumann boundary conditions meet due to the appearance of a
153 singularity (**?**). This singularity was reviewed extensively in the past (**?????**) but the studies
154 where this singularity appears in the bubble dynamics problems are rare. The asymptotic

155 solutions close to the point where homogeneous Dirichlet and Neumann boundary conditions
156 meet can be alternatively expressed using the general solution of the 2D Laplace equation
157 (**???**) and takes the form of

$$\tilde{p}_s = \sum_{k}^{\infty} C_k \tilde{r}_s^{b_k} \cos\left(b_k \theta_s\right), \tag{3.2}$$

159 where $\tilde{r}_s = r_s/R_c$ is the nondimensional distance from the contact line and $b_k = \frac{\pi}{\alpha}(k + 1/2)$.
160 Taking the derivative with respect to the normal of the interface we readily find the interface
161 acceleration magnitude near the contact line as

$$|a_I| = \frac{1}{\rho}|\frac{\partial p}{\partial n}| \approx a_0 C_0 b_0 \tilde{r}_s^{b_0-1}, \tag{3.3}$$

163 where $a_0 = \frac{p_\infty - p_{0,L}}{\rho R_c}$ is the acceleration magnitude for a spherical bubble. This expression
164 exhibits a singularity at the contact point ($r_s \rightarrow 0$) when $b_0 = \frac{\pi}{2\alpha} < 1$ (or $\alpha > \pi/2$) implying
165 that the acceleration at the triple contact point is infinite. In these conditions the first term in
166 the expansion is the leading order term that eventually dominates the solution in the region
167 $r_s \leqslant R_c$. This can also be clearly seen in figure 2b where the fitting curve shown with
168 solid line is obtained using the first term of the series solution (i.e. parameters C_0 and b_0
169 in equation 3.3). We repeat the fitting procedure for various α to verify that the numerical
170 values of b_0 match well with theoretical predictions and find C_0 which is a constant of order
171 one that slightly increases with α (figure 3a). Note that for non-singular problems, $\alpha < \pi/2$,
172 the first term in the series is not necessarily the leading order term and therefore alternative
173 expansions of the solution should be used to describe the dynamics of these bubbles. In
174 this manuscript, we will focus on the characterization of the regimes where the singularity
175 appears.

176   Figure 3b depicts the local non-dimensional acceleration magnitude at bubble interface
177 $\tilde{a}_I = |a|/a_0$ parametrized with the angle θ_w for four representative cases with $\alpha =$
178 $\pi/3, \pi/2, 2\pi/3, 3\pi/4$. As expected, in the case of $\alpha = \pi/2$, the numerical solution recovers
179 the Rayleigh-Plesset solution and the non-dimensional acceleration is uniform and equal to
180 one all over the interface. When $\alpha < \pi/2$ the interface acceleration (thus velocity) tends to
181 zero at the contact point, and therefore it seizes to move even in the potential flow problem
182 with a slip wall. For $\alpha > \pi/2$, the appearance of the singularity is evident from same figure.
183 Dotted lines are used to show the numerical solution while solid lines show result of equation
184 3.3 evaluated at the interface, which shows excellent agreement close to the contact point,
185 i.e. small values of θ_w. Near the axis of symmetry (e.g. $\theta_w \rightarrow \pi/2$ and $\tilde{r}_s \approx 1$), the errors are
186 visible and the first term in the series does not suffice to describe accurately the acceleration
187 field.

188 ### 3.1.2. *Far field solution*

189 The far field flow created by the bubble corresponds to a punctual sink sitting at the
190 intersection between the wall and the axis of symmetry. The integration of the momentum
191 equation in the radial coordinate provides the magnitude of pressure gradient generated by a
192 punctual sink at an arbitrary distance from the sink as

$$\left|\frac{d\tilde{p}_{\text{far}}}{d\tilde{r}_w}\right| = \frac{|\overline{a}_I|}{a_0} \frac{(1 + \cos(\alpha))}{\tilde{r}_w^2}, \tag{3.4}$$

194 where $|\overline{a}_I|$ is the magnitude of averaged acceleration along the interface, which determines
195 the strength of the punctual sink. Figures 1c clearly shows that this equation captures well
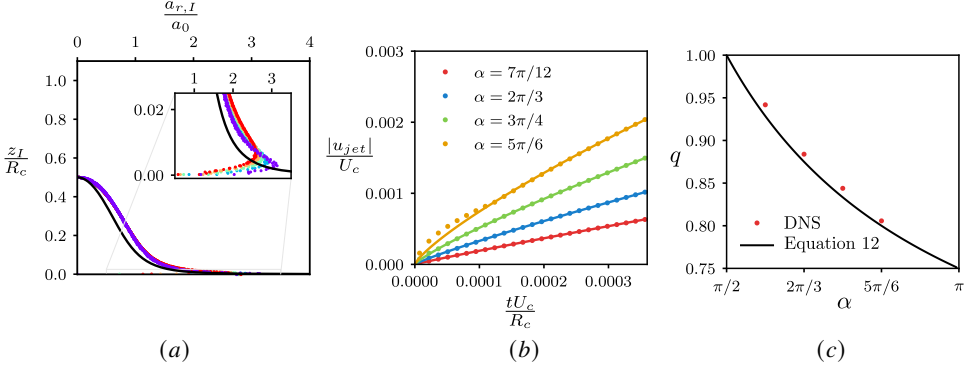196 the decay of the pressure gradient with the distance $\tilde{r}_w$ far from the interface. Because the

Figure 4: (a) Results from the DNS solution for $\alpha = 2\pi/3$ and $Re = 100$. Mean interface acceleration in direction parallel to the wall, $a_{r,I} = u_{r,I}/t$, as a function of the distance from the wall at different times (in color). For reference we include the potential flow solution given by Eq. 3.3 evaluated at the interface (solid black line). The inset represents a zoom into the viscous boundary layer generated close to the wall. (b) Evolution of jet velocity for different contact angles from (dots) DNS and (solid lines) fitting using Eq. 3.6 . (c) Exponent q from DNS fitting and predictions of Eq. 3.7.

197 first term of the series in equation 3.3 predicts the interface acceleration reasonably well, we
198 obtain an estimation of the averaged acceleration magnitude for bubbles with $\alpha > \pi/2$ as

$$|\overline{a}_I| = \left| \frac{1}{S_b} \int \frac{-1}{\rho_l} \frac{\partial p}{\partial n} dS_b \right| = a_0 C_0 b_0 G(\alpha), \tag{3.5}$$

200 where S_b stands for the bubble interface surface and $G(\alpha)$ is a geometrical factor that can be
201 numerically computed assuming that the first term in the series is indeed the leading order
202 term along the entire bubble interface. Figure 3c shows that the averaged nondimensional
203 interface acceleration magnitude obtained using this model, which compares well with the
204 full numerical results of the free surface model and the DNS solution of the (both viscous
205 and inviscid) Navier-Stokes equations. The results of the simplified model are obtained using
206 the value of C_0 numerically computed and reported in figure 3a. For $\alpha > \pi/2$, $|\overline{a}|$ increases
207 with α. The three proposed models agree well for the angles tested implying that the free
208 surface model as well as the simplified expression given in equation 3.5 capture well the
209 averaged bubble response at short times for sufficiently large Reynolds numbers.

210 ### 3.2. *Viscous correction*

211 The potential flow solution is only formally exact at the initial time $t = 0$ when the interface
212 is at rest, as soon as the interface is set into motion a thin boundary layer immediately
213 develops regularizing the flow close to the contact point. We use the results from the DNS
214 of the Navier–Stokes equations at short times to investigate the influence of viscosity on the
215 dynamic response of the bubbles
216 Since we know that at short times the velocity is linearly related to the acceleration i.e.
217 $u_r = a_{r,0}t$, we plot in figure 4a the evolution of the averaged interface acceleration magnitude
218 parallel to the wall as a function of the normal distance from the wall obtained from DNS
219 for $\alpha = 2\pi/3$, $Re = 100$ and small values of the non-dimensional time tU_c/R_c shown in
220 color. The inset figure shows the clear development of a boundary layer very close to the
221 wall, where the maximum velocity defines the thickness of this layer. Outside this region
222 the free surface potential flow solution shown with a solid black line (Eq. 3.3) predicts the
223 interface velocity obtained from DNS relatively well. Inside the viscous boundary layer, the
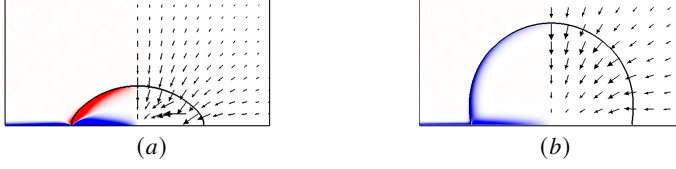224 interface acceleration is sensitive to the slip length imposed (see Appendix A) and also to

Figure 5: The vorticity in color map and velocity vectors obtained from DNS after short time short time ($\frac{tU_c}{R_c} = 0.11$) for Re = 1000 for (a) $\alpha = 2\pi/3$ and (b) $\alpha = 5\pi/12$.

the movement of the contact line. In this region, the solution of free surface model at $t = 0$ cannot be extrapolated to predict the flow field near the contact line at short but finite times.

Remarkably, although the contact line motion is grid dependent, the average acceleration and the maximum jet velocity is shown to be independent of the slip length imposed (see Appendix A). This fact together with slight dependence of the average acceleration with Re (figure 3c) confirms that for large enough Reynolds numbers, the bubble dynamic response is mainly governed by the potential flow solution. In these conditions, the free surface potential flow model at $t = 0$ is a useful tool to predict the average dynamics of the interface at small times.

The maximum interface velocity magnitude is fitted from DNS data and used to characterize the jet velocity $|u_{jet}|$ (figure 4b) using a power law function

$$\frac{|u_{jet}|}{U_c} = A \left(\frac{tU_c}{R_c} \right)^q . \tag{3.6}$$

A theoretical estimation of coefficients A and q can be obtained from the singular solution described in the previous section as follows: The jet velocity after small time (t_s) can be approximated from the initial acceleration evaluated at the interface at height equal to thickness of boundary layer $z = \delta(t_s)$. The δ is given approximately by the solution of the Stokes problem for the flow near the flat plate that is impulsively started from rest therefore, we can impose that $\delta(t_s) \approx C_\delta \sqrt{\nu t_s}$ where C_δ is a constant of order unity. In this case the jet velocity velocity is estimated as

$$u_{jet}(t_s) = a_{r,I} \left(t = 0, z_I = \delta(t_s) \right) \, t_s$$

where we assume that the interface quickly decelerates as soon as it enters inside the viscous boundary layer. Thus, the coefficient q is readily obtained as

$$q = \frac{1}{2} + \frac{\pi}{4\alpha}. \tag{3.7}$$

As shown in Figures 4c this model is capable of capturing the evolution of the jet velocity at small times found from DNS simulations for $\alpha > \pi/2$. The exponent q (figure 4c) decreases as α increases because the acceleration gradient in the normal direction increases with α as seen in figure 3b. Note that $q < 1$ for $\alpha > \pi/2$ and therefore the jet acceleration is singular at $t = 0$ even in the presence of viscous effects.

To describe the dynamics of the bubble, it is useful to discuss the influence of vorticity generated during the collapse which at short times is concentrated in a sheet vortex at the interface. By assuming zero stress condition at the interface for $t = 0$, the only non-zero component of the vorticity can be written as

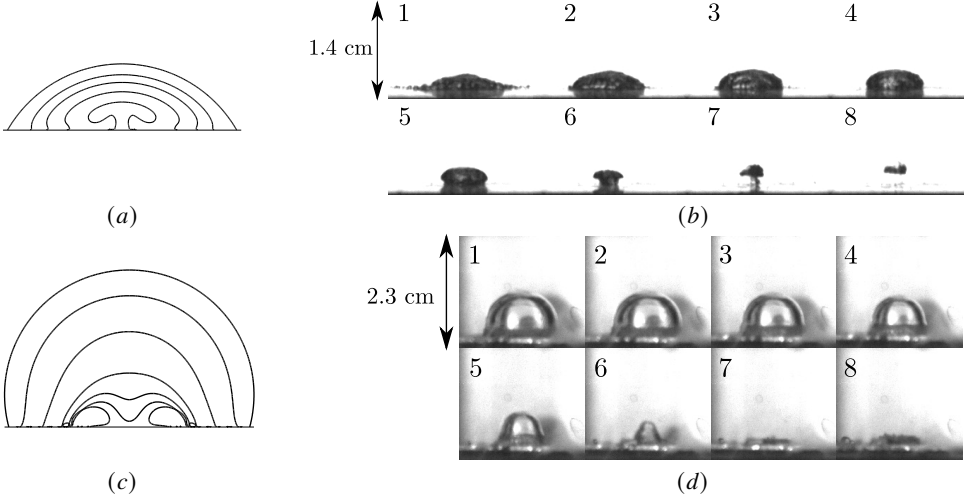$$\omega_\phi = -2 \frac{\partial u_r}{\partial \theta}.$$

Figure 6: Representative examples of the bubble response for (top row) $\alpha > \pi/2$ and (bottom row) $\alpha < \pi/2$ obtained (left column) from DNS at long times and (right column) representative experiments of the collapse of a bubble in contact with a wall using a laser pulse. (a) Interface contours for $\alpha = 2\pi/3$ ($\frac{tU_c}{R_c} = 0, 0.12, 0.16, 0.19, 0.23$) (b) Images from experiments taken every 0.125 ms for $\alpha > \pi/2$. (c) Interface contours for $\alpha = 5\pi/12$ ($\frac{tU_c}{R_c} = 0, 0.2, 0.29, 0.33, 0.35, 0.35, 0.37$). (d) Images from experiments taken every 0.125 ms for $\alpha < \pi/2$.

It follows from the potential flow solution (figure 3b) that the sign of the acceleration gradient changes depending on the initial contact angle is greater or less than $\pi/2$, reverting the sign of the vortex sheet generated at the interface. This behavior is indeed observed from the numerical simulations as shown in figure 5 (a and b), where the strength of the vortex sheet is plotted with saturated color maps. The change in dominant color represents the opposite sign of vorticity at interface between the two cases. Thus, we can conclude that similar to the background potential flow, viscous effects induced by the diffusion of vorticity from the interface also favor the appearance of a annular jet parallel to the wall for $\alpha > \pi/2$.

4. Long time dynamics

After describing the short time dynamics, we investigate the long time consequences of this singular response using DNS. The solver proposed is described in (**?**) [CITE BASILISK] and summarized in Appendix B. We solve equations 2.1-2.1, where for the sake of simplicity, we neglect surface tension effects, as we are interested in regimes with large characteristic Weber numbers.

The bubble interface at various times obtained from DNS is shown in figure 6 (a and c) for $Re = 1000$ and two representative cases with initial contact angles: $\alpha = 5\pi/12$ and $2\pi/3$. For $\alpha = 2\pi/3 > \pi/2$ the highest interface velocity is developed at edge of the viscous boundary layer and an annular jet is generated parallel to the wall leading to a mushroom-like shape (figure 6 a). This behavior can be reproduced experimentally (figure 6 b) using the setup described briefly in appendix B and also in references (**??**), where a laser pulse induces a shock wave in aluminum plate that leads to the appearance of a flat bubble with shape similar to spherical cap at maximum volume. The results are consistent with previous numerical works (**??**) yet its origin and consequences of this behavior were not explained. Remarkably, when the collapse is strong enough and the jet reaches the axis of symmetry,
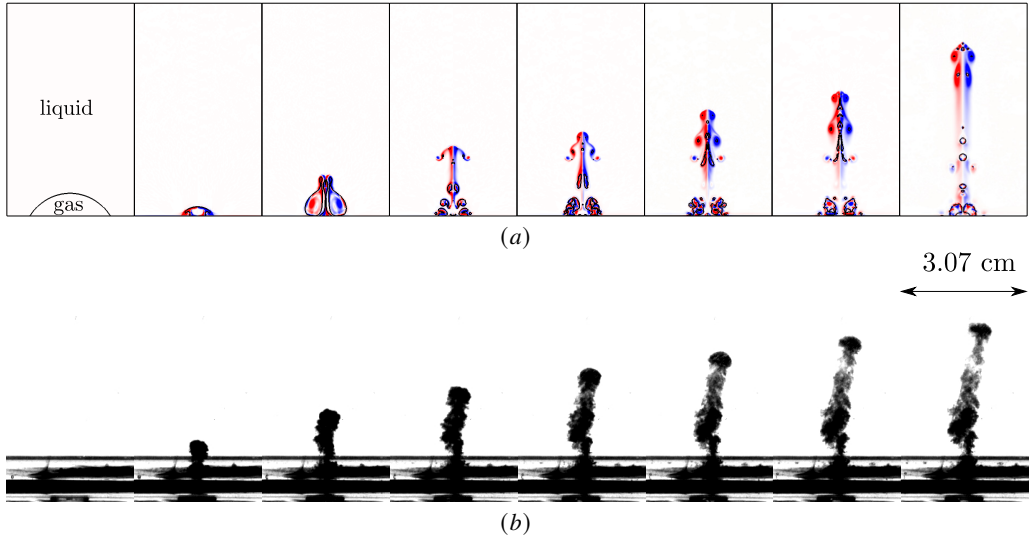
(a)

3.07 cm

(b)

Figure 7: (a) Bubble interface in black curve and the vorticity field in the colormap as obtained from DNS is shown at (consecutively from left to right) $\frac{tU_c}{R_c} = 0, 0.19, 0.3, 0.81, 1.00, 1.45, 1.95, 4.90$. An the annular jet parallel to wall reaches the axis resulting in to the jet directed away from the wall which later generates the vortex ring. The results are plotted for $\alpha = 2\pi/3$ and Re $= \infty$ (b) The visualization of liquid flow field obtained by adding dye at the bottom of tank resulting from collapse of bubble is shown at every 2.5ms.

a stagnation point appears and secondary upward jet normal wall is generated. Such a jet is not conventional in cavitation and generate vortex ring structures similar to those observed by **?** which are persistent in nature and can travel large distances in comparison to bubble size, thus have long-range effects. The generation of this vortex ring is illustrated numerically in figure 7a where the color maps show the vorticity field. Experimentally we visualize the appearance of this phenomenon by adding the dye in the bottom of the tank (figure 7b) during the collapse of a flat bubble. If the vortex dipole reaches a free surface, a jet is observed at the free surface which is significantly delayed with respect to the instant of the bubble collapse.

In the case $\alpha = 5\pi/12 < \pi/2$ the interface acceleration is minimum at the contact line and maximum at the tip of the spherical cap leading to a conventional high–speed liquid jet directed towards the wall (figure 6 c). These conditions are reproduced experimentally (figure 6 d) using a classical experiment where a laser is focused in the liquid very close to the wall. Similar dynamics have been described in previous theoretical, experimental as well as numerical studies (**???**).

In conclusion, we show that the effective contact angle at the instant of maximum expansion controls the acceleration at short times after beginning of the collapse phase and the jetting direction at longer time scales, significantly modifying the nature of interaction between the bubble and the surrounding medium. This change of behavior is shown to be related to the appearance of a singularity in potential flow solution at $t = 0$ for $\alpha > \pi/2$, which causes extremely high accelerations close to the contact point and a change in vorticity direction with respect to the $\alpha < \pi/2$ case. Thus, the bubble shape at the instant before collapse turns out to be critical if one wants to control or model the physical phenomena triggered by the collapse of bubbles attached to a wall.

The unconventional jetting mechanism observed for collapse of bubble with $\alpha > \pi/2$ can be used to explain and control mixing and transport processes of pollutants and drugs induced

Rapids articles must not exceed this page length

by bubble dynamic processes. While the former finds direct application in the understanding of many transport processes in nature, the later has direct implications in the development of treatment technologies based on the interactions between bubbles and tissue including drug delivery and high intensity ultrasound techniques (**???**). This particular behavior may be also behind the mechanism of delayed surface jets at the free surface mentioned by Kedrinskii **?**. Another exciting phenomenon is generation of surface waves from the bubble collapse in deep water. The phenomenon described in this manuscript may be eventually related to the appearance of Tsunamis from underwater volcanic eruptions where the mechanisms linking both processes are not fully understood yet **?**. Finally the fundamental understanding of interaction of collapsing bubble with the surrounding media should improve the design and development of various technologies based on the physical, mechanical and chemical effects induced by the collapse of bubbles. The relation of the singularity of potential flow to the well known force singularity during the motion of contact line **?** remains another open research problem where the solutions reported in this work may inspire new ideas.

Appendix A. Convergence study

The convergence properties of the contact line velocity and jet velocity are discussed in this section. The velocity of the contact line (figure 8 top where u_{TP} is contact line velocity) changes as the mesh is refined since slip length changes implicitly ($\lambda = \Delta x_{min}/2$). It is also evident from the same plot that in very short times the well known scaling for the thickness of the boundary layer ($t^{1/2}$) is not recovered as the boundary layer is not well resolved. At slightly longer times the boundary layer growth recovers the expected scaling law. Despite of the sensitivity of the contact line motion to the slip length imposed, the peak interface velocity (jet velocity u_{jet}) plotted in Figure 8 bottom reveal that the numerical results are converged and therefore independent of the slip length.
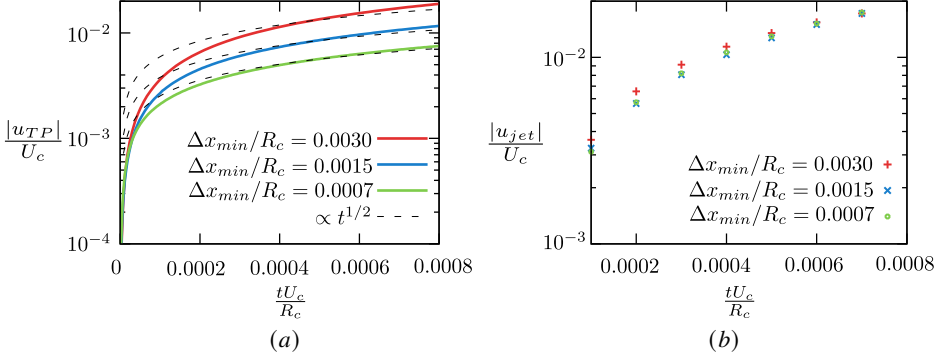
Figure 8: The grid convergence of viscous solution Top: The evolution of velocity of contact line is plotted for different grid-size. Bottom: The evolution of jet velocity is plotted for various grid size.

Appendix B. Methodology

B.1. *Numerical tool*

The numerical results are obtained using the free and open-source PDE solver Basilisk [CITE BASILISK]. The Laplace equation is solved using the multigrid solver in basilisk with mesh refined near the bubble. The spherical cap shapes are generated using immersed boundary implementation available in the code.

The Euler equations and viscous solutions are solved using the All-Mach implementation (**?**), where one fluid approach is used to solve the modeling equations. The spherical cap-shaped bubble is initialized in a square domain of size 100 times the initial radius of curvature of this bubble. The simulations are axisymmetric, with the right boundary being the axis of symmetry, with the bubble is attached to the bottom boundary where either an impermeable free slip wall or Non-slip boundary conditions are applied when we consider Euler and viscous solution respectively. The left and top boundaries are given constant far-field pressure conditions and Neumann conditions for velocity. The grid is refined progressively near the interface to a minimum grid size of $\Delta x_{min}/R_c = 0.00152$ (for Euler) and 0.00038 (for Navier-Stokes) times the radius of curvature for studying short time dynamics. The long time scale simulations are carried out with same setup and using adaptive mesh refinement with smallest grid size $\Delta x_{min}/R_c = 0.0061$. The maximum time step in the simulation is governed by acoustic CFL restriction, which in our case is 0.4.

B.2. *Experimental method*

The experiments are performed with pulsed Nd:YAG laser (model quanta ray pro 350-10) that provides maximum of 3.5J of energy with Gaussian distribution in time having half maximum at 9.2 ms. This laser beam passes through a quarter wave plate and polarizer for modulating the energy and then focused using a planoconvex lens of focal length 250mm that creates a focal spot of 4mm in diameter on the aluminum plate. For bubbles shown with $\alpha > \pi/2$ the laser is focussed on the water droplet attached to bottom of an aluminum plate (1 mm thick) kept at bottom of a water tank and for the bubbles with $\alpha < \pi/2$ the laser if focussed on the top of this aluminum plate kept at the bottom of same tank. The laser energy is set to 50% of maximum in case where $\alpha < \pi/2$ and we observe the cavitation phenomenon in the water tank using high speed camera.